Nanoscale heterogeneity promotes energy dissipation in bone

KUANGSHIN TAI[1]*, MING DAO[1]*, SUBRA SURESH[1,2], AHMET PALAZOGLU[3] AND CHRISTINE ORTIZ[1]†

[1]Department of Materials Science and Engineering, Massachusetts Institute of Technology, 77 Massachusetts Avenue, Cambridge, Massachusetts 02139, USA
[2]Division of Biological Engineering, Massachusetts Institute of Technology, 77 Massachusetts Avenue, Cambridge, Massachusetts 02139, USA
[3]Department of Chemical Engineering and Materials Science, University of California, One Shields Avenue, Davis, California 95616, USA
*These authors contributed equally to this work
†e-mail: cortiz@mit.edu

Published online: 21 May 2007; doi:10.1038/nmat1911

Nanomechanical heterogeneity is expected to influence elasticity, damage, fracture and remodelling of bone. Here, the spatial distribution of nanomechanical properties of bone is quantified at the length scale of individual collagen fibrils. Our results show elaborate patterns of stiffness ranging from ~2 to 30 GPa, which do not correlate directly with topographical features and hence are attributed to underlying local structural and compositional variations. We propose a new energy-dissipation mechanism arising from nanomechanical heterogeneity, which offers a means for ductility enhancement, damage evolution and toughening. This hypothesis is supported by computational simulations that incorporate the nanoscale experimental results. These simulations predict that non-uniform inelastic deformation over larger areas and increased energy dissipation arising from nanoscale heterogeneity lead to markedly different biomechanical properties compared with a uniform material. The fundamental concepts discovered here are applicable to a broad class of biological materials and may serve as a design consideration for biologically inspired materials technologies.

Bone, like many natural materials, is inherently structurally, and hence mechanically, heterogeneous owing to spatial distributions in the shape, size and composition of its constituent building blocks. Heterogeneity also arises from a multitude of different types of biomacromolecule, pores containing fluids of variable viscosities and numerous interfaces (for example solid–solid, solid–fluid, damage based)[1,2]. As a consequence of the hierarchical nature of bone[3], mechanical heterogeneity is expected to exist at multiple length scales. Macroscopically, significant variations in mechanical properties have been observed for different anatomical locations[4], as well as for regions within a particular anatomical location[5], and are thought to develop in response to distinct loading requirements[6]. At the microscopic level, instrumented indentation has further identified differences in moduli and hardness for specific features such as trabeculae, interstitial lamellae and thick and thin lamellae in osteons, which have been attributed to collagen fibril orientation and anisotropy, as well as variations in mineral content[7,8]. Heterogeneity at this length scale is also expected to arise from the continual cellular remodelling processes resulting in a mixture of 'old' and 'new' bone at any given time. For example, osteonal bone typically undergoes substantial remodelling, whereas older interstitial bone[9] has a higher degree of mineralization[10], leading to increased stiffness[8]. Atomic force microscopy (AFM)-based nanoindentation has been used to distinguish mechanically heterogeneous microscale regions in bone tissue from genetically modified mice with various levels of transforming growth factor, TGF-β, which correlate with compositional heterogeneity measured by Raman microspectroscopy, and additionally has been shown to possess the capability for quantifying nanoscale heterogeneity[11]. All of these studies have ignited speculation on the role of heterogeneity in strain concentration, fracture risk, adaptation and damage accumulation[8,11–16]. They also raise important issues as to whether heterogeneity is advantageous or disadvantageous to the mechanical function of bone[2]. Detailed and quantitative studies of the consequences of heterogeneity, in particular at the nanoscale, on the structural integrity and proper function of the tissue are largely unknown.

In this paper, we first quantify mechanical heterogeneity at nanometre length scales. Here, the mechanical response arises from an individual mineralized collagen fibril within the bone extracellular matrix, which is composed of platelike carbonated apatite mineralites (~tens of nanometres in length and width, and 3–5 nm in thickness[1]) that permeate in and around type-I collagen in an overlapping manner[17], as well as a small concentration of ~200 different types of non-collagenous protein (<10 wt% of total protein)[1]. It has become increasingly evident that the unique nanoscale properties of bone play a key role in its macroscopic biomechanical function[17–22], as this is where inelastic deformation and fracture must first initiate. Furthermore, because osteocytic processes have dimensions that are of the nanometre length scale[23], nanoscale heterogeneities in material properties of the surrounding extracellular matrix would be expected to modulate local stresses, thereby potentially influencing processes such as remodelling, migration and adhesion.

Nanoindentation using a spatially controlled AFM-based instrument was carried out with a sharp tetrahedral silicon probe tip (end radius ~ 15 nm, as estimated by high-resolution scanning electron microscopy imaging and AFM imaging of a gold-nanoparticle calibration standard) in ambient conditions as shown in Fig. 1 (see the Methods section). This instrument has a fully three-dimensional (3D) closed-loop piezoelectric displacement system that ensures positional accuracies in three dimensions of <1 nm. Grids of indentations over a 2 μm × 2 μm area were carried out on adult bovine tibial cortical bone (prepared with no alcohol

dehydration, embedding or chemical fixation) both perpendicular and parallel to the long bone axis, where the separation distance between the indents was 100 nm. This value was chosen to avoid overlap of neighbouring inelastic strain/residual stress zones estimated by appropriate finite-element analysis (FEA) simulations as detailed in the Methods section. Inelastic deformation is predicted by FEA simulations (data not shown) to take place almost immediately after contact owing to the high local stress concentrations due to the sharpness of the probe tip, which is consistent with a finite residual depth observed experimentally on unloading (as will be shown later on). Hence, this size of the inelastic strain/residual stress zones determines the 'spatial resolution' of the experiments or the interindent spacing, that is, it is not limited by instrumental factors, only by the sample deformation. The deformation of the probe tip is negligible, because the elastic modulus of silicon is approximately one order of magnitude greater than that of bone. The deformation of the instrument was negligible (compliance $\sim 3 \times 10^6\,\mathrm{N\,m^{-1}}$) compared to the deformation of the cantilever (spring constant $\sim 56.2\,\mathrm{N\,m^{-1}}$). It was ensured that during indentation the laser spot was maintained within the linear range of the position-sensitive photodiode. The maximum indentation depth was <40 nm at a 5 μN maximum load (for ~90% of all of the experimental data), corresponding to an elastic-zone radius (containing the inelastically deformed region) of ~70 nm (estimated by FEA simulations; see the Supplementary Information). As type-I collagen fibrils in these types of bone sample were measured to have a mean diameter of ~150 nm (ref. 24), the deformation induced by indentation was on the length scale of an individual collagen fibril. At each position in the grid, the unloading slope of the force-versus-displacement curve was used to calculate an indentation modulus on the basis of a widely used contact mechanics model[25] (see the Methods section). Owing to the assumptions of this model and the hierarchical structure of bone, the extracted indentation-modulus values reflect relative mechanical stiffness and are not absolute quantitative values. However, the relative spatial differences in stiffness can be accurately compared. Two-dimensional (2D) contour maps of local stiffness were constructed, which enabled the direct visualization of nanomechanical spatial heterogeneity. These maps were compared with high-resolution a.c. intermittent contact-mode topographic AFM images of the same area of the bone ultrastructure taken before indentation.

The ultrastructure of osteonal bone viewed perpendicular to the long bone axis showed a nanogranular morphology of a dense array of mineralites (Fig. 2a) with an average maximum lateral dimension of 64.9 ± 26.4 nm, peak-to-valley height of 11.5 ± 9.1 nm and r.m.s. surface roughness of 11.5 nm calculated over the entire 2 μm × 2 μm scan (measured from corresponding height images). Distinct type-I collagen fibrils and their characteristic 67 nm periodicity were not observed owing to the dense array of mineralites present. However, as reported previously[24], AFM imaging after partial demineralization, using a one-second etch in ethylenediaminetetraacetic acid, reveals a surface of type-I collagen fibrils with varying degrees of orientation within the sample plane, the expected 67 nm banding and a mean diameter of $\sim 151 \pm 17$ nm. The stiffness map for the loading axis perpendicular to the long bone (osteonal) axis (Fig. 2b) corresponding to the area imaged in Fig. 2a shows a distribution with values ranging from 2 GPa (white) to 26 GPa (black) with an averaged indentation-modulus value of 8.55 ± 3.7 GPa and coefficient of variation or COV (ratio of the standard deviation to the mean) of 0.43. Individual force versus depth curves corresponding to a few of the positions shown in Fig. 2b are given in Fig. 2c and show finite residual depth after unloading ranging from 17 to 27 nm, indicating the presence of inelastic deformation. This

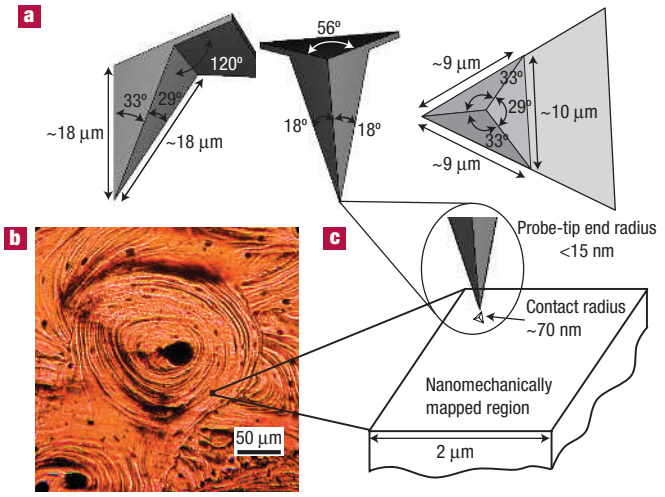

Figure 1 Schematic diagram of experiment used to quantify nanomechanical heterogeneity in bone. a, 3D schematic diagrams illustrating probe-tip geometry and dimensions from the side and back view (left), front view (middle) and bottom view (right) as determined by scanning electron microscopy. **b**, Optical microscopy image of an individual osteon in adult bovine cortical bone showing the Haversian canal, circumferential lamellae and the lacuno-canalicular porosity. **c**, Schematic diagram of a 2 μm × 2 μm region probed nanomechanically drawn to scale relative to osteon size; the size of the indented region is also drawn to scale.

is due to the large stress concentrations imparted by the very small probe tip which initiates inelastic deformation almost immediately on contact (as verified both experimentally and computationally, data not shown). A curved region of lower stiffness appears diagonally across the mapped region (length ~ 1.8 μm), whereas higher-stiffness regions appear horizontally across the top of the mapped region (Fig. 2b). Smaller localized variations and gradients occur throughout the map as well.

Multiple mapping experiments were carried out on bones from five different animals and nanoscale heterogeneity was found to exist in all samples, with COV values ranging from 0.26 to 0.46 (data not shown). The fine patterns of each stiffness map varied among different animals (data not shown), as well as the mean stiffness values (ranging from 8.5 ± 3.7 to 14.6 ± 5.0 GPa), as expected. We also investigated the effect of surface roughness by carrying out >3,000 indentation experiments over a range of maximum depth, h_{max}/r.m.s. surface roughness (where the r.m.s. surface roughness was measured directly at every position using a.c. intermittent contact-mode AFM height images). It was found that the COV stayed within 0.3–0.4 for the entire range of h_{max}/r.m.s. surface roughness ~2–16 and was statistically independent of h_{max}/r.m.s. surface roughness as assessed by an analysis of variance test using the O'Brien method to test for homogeneity of variances between the different COV groups relative to one another. Using this analysis, it was shown that the assumption for homoscedasticity was met ($F = 1.0113$, $p > 0.05$), that is, that there was no overall statistically significant trend for the dependence of the COV on h_{max}/r.m.s. surface roughness (see the Supplementary Information).

Assuming a helicoidal collagen fibril arrangement[26] and transversely isotropic properties of individual collagen fibrils[27], variations in collagen fibril orientation are not expected to play a major role in the observed heterogeneity, because the loading axis is perpendicular to the collagen fibril axis. Other possible sources of observed heterogeneity include

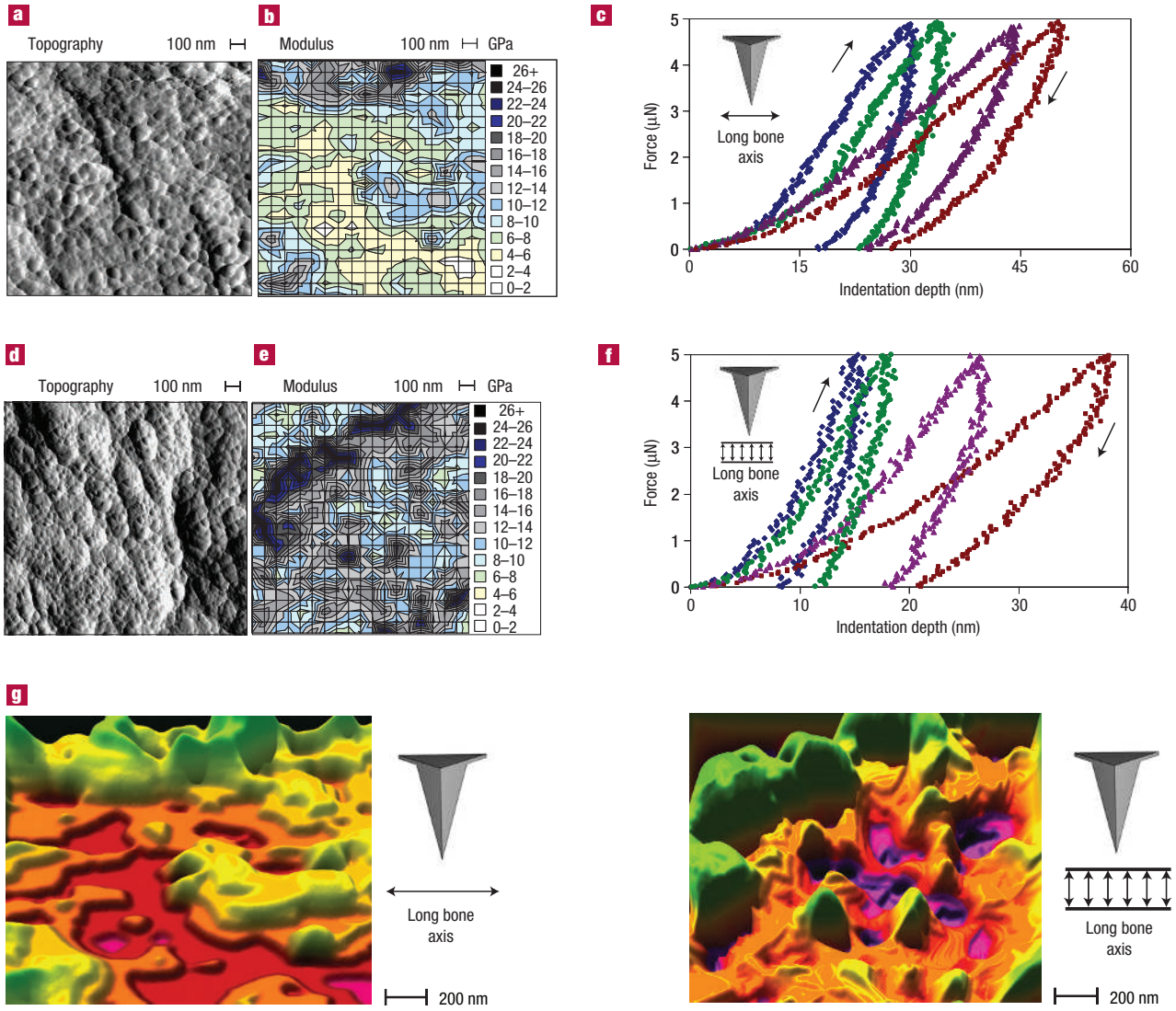

Figure 2 The ultrastructure and nanomechanical spatial heterogeneity of bone stiffness. a, An a.c. intermittent contact-mode AFM amplitude image viewed perpendicular to the long bone axis. **b**, 2D contour map of modulus reduced from nanoindentation data[25] for the area shown in **a** with loading axis perpendicular to the long bone axis. **c**, Individual nanoindentation curves at different locations within the modulus map **b**; moduli (GPa) blue diamonds 12.5, green circles 10.5, purple triangles 5.4, brown squares 4.2. **d**, An a.c. intermittent contact-mode AFM amplitude image parallel to the long bone axis. The average maximum lateral dimension measured from corresponding AFM height images was determined to be 64.9 ± 26.4 nm, which is consistent with the known dimensions of mineral particles in bone and other calcified tissues, as measured by scanning electron microscopy[50], transmission electron microscopy[51] and small-angle X-ray scattering[52]. These values are somewhat smaller than those previously observed on similar samples[20] owing to optimization of the experimental imaging protocol to achieve higher resolutions. **e**, 2D contour map of modulus for the area shown in **d** with loading axis parallel to the long bone axis. **f**, Individual nanoindentation curves at different locations within the modulus map **e**; moduli (GPa) blue diamonds 24.2, green circles 18.1, purple triangles 15.8, brown squares 5.7. **g**, 3D graphic illustrations of the modulus maps shown in **b** (left), where loading was carried out perpendicular to the long bone axis, and **e** (right), where loading carried out parallel to the long bone axis. The vertical axis corresponds to stiffness, where the highest vertical topography corresponds to the maximum value and the lowest topography corresponds to the minimum value. For **b** and **e**, in the 26+ bin 1.5% of the data points showed moduli > 28 GPa.

nano- to microscale organic–inorganic compositional or structural variations (for example, different sizes, shapes and/or spacing between nanoscale constituents). Compositional fluctuations are known to exist down to ~1 μm, as revealed by micro-Raman spectroscopy[28].

Indentation-modulus data taken with the loading axis parallel to the long bone axis on the same sample show less heterogeneity (coefficient of variation of 0.37), with values ranging from 5 (light yellow) to 31 (black) GPa and increased mean stiffness ($\sim 12.9 \pm 4.8$ GPa) (Fig. 2d–f) compared with the perpendicular orientation (by a factor of ~1.5). This trend is consistent with macroscopic tissue-level data[5] and collagen fibril anisotropy (increased stiffness along the fibril axis compared with transverse directions)[27]. A large curved region is observed with increased stiffness (thickness ~250 nm) in the upper left hand side of the map, as well as the lower right hand side (distance between high stiffness regions ~1.5 μm). Similar experiments were carried out on five different osteonal regions of the same bone sample. Nanoscale mechanical heterogeneity was observed in all of these maps and showed COV values ranging from 0.37 to 0.43 (data not shown). Again, the fine

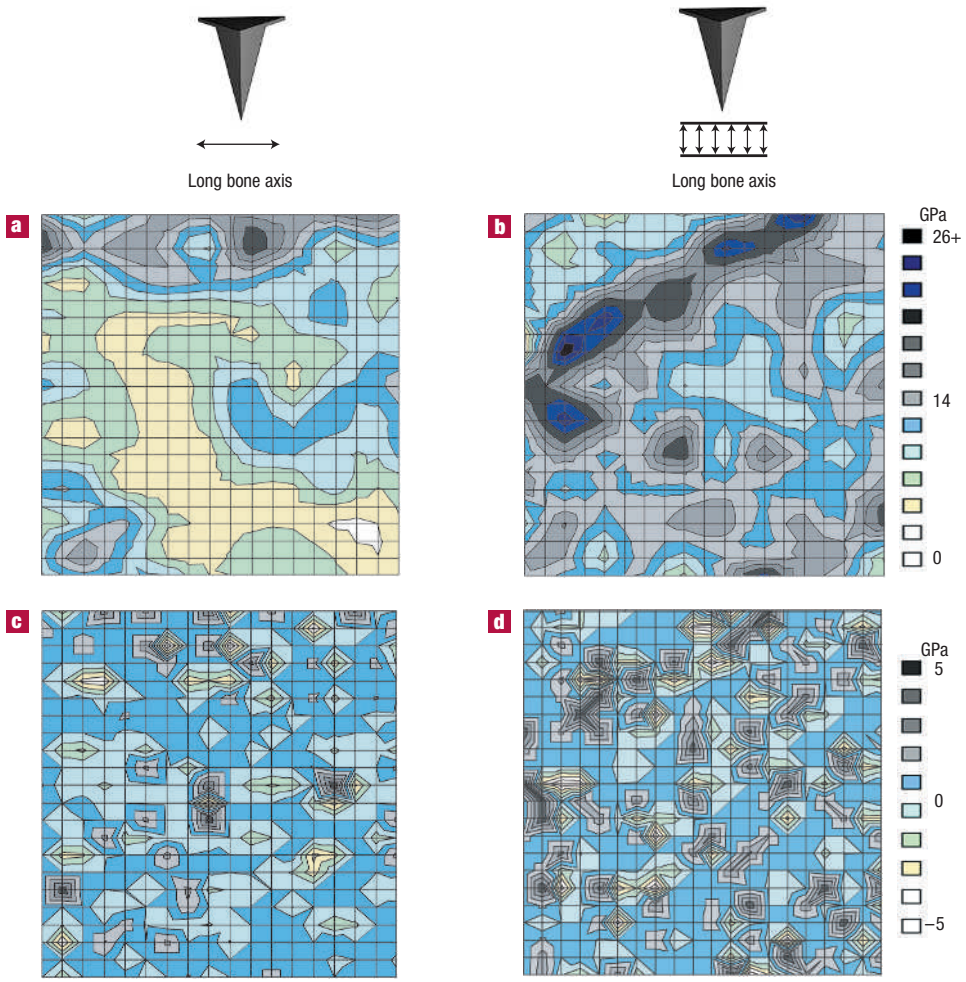

Figure 3 Quantitative analysis of nanomechanical-property maps using discrete wavelet transform. **a**, Level-1 approximation for modulus map given in Fig. 2b (loading axis perpendicular to the long bone axis). **b**, Level-1 approximation for modulus map given in Fig. 2e (loading axis parallel to the long bone axis). **c**, First-level detail corresponding to **a**. **d**, First-level detail corresponding to **b**.

patterns of each stiffness map varied among different regions and the mean stiffness values ranged from 11.8±3.6 to 14.1±5.3 GPa. Figure 2g provides a 3D visualization of the nanoscale stiffness data, with the vertical direction corresponding to the stiffness magnitude, comparing the parallel and perpendicular orientation directions. Although the COV for the contour map perpendicular to the long bone axis is greater, the differences in peak-to-valley modulus values are more apparent for the map from indents taken parallel to the long bone axis in the 3D visualizations. Assuming the spiral model for collagen fibril orientation[29], this occurrence may arise from off-axis loading of collagen fibrils, as opposed to in-plane loading in the perpendicular orientation. If the heterogeneity observed (for loading parallel to the long bone axis) was solely due to collagen fibril orientation, a more-or-less-continuous stiffness gradient would be observed, which does not seem to be the case here. Thick and thin lamellae have been measured to be approximately ∼5−7 and 1 μm in width, respectively[30], with the thin lamellae being ∼10% softer than the thick ones[8]. No distinct patterns were observed that could be conclusively associated with such features. Hence, the fluctuations observed must partially originate from smaller-length-scale features.

The modulus maps were analysed quantitatively using the discrete wavelet transform[31], where decomposition of spatial frequencies creates a coarser approximation of the image (see the Methods section). Details can be associated with a 'pseudofrequency' that identifies the length scales of the patterns removed at spatially specific regions. Figure 3a,b depicts the first-level approximations of the original images corresponding to indents perpendicular and parallel to the long bone axis, respectively. The details for these corresponding maps were removed to obtain the coarser image (Fig. 3c,d). The detail images show largely random features that prevail at the high spatial frequencies. However, they also capture specific patterns associated with the high-modulus areas. One can observe high-modulus peaks that coincide with the larger high-modulus domains (more apparent with the image parallel to the bone axis, Fig. 3d). The first level of decomposition thus seems to remove the local high-modulus peaks, leaving broader regions of stiffness. The characteristic length scale given by the pseudo(-spatial-)frequency analysis, identified as ∼156 ± 28 nm, corresponds closely to the experimentally measured mean diameter of an individual collagen fibril[24].

The mechanical heterogeneity described above for the AFM-based nanoindentation is much more pronounced compared with depth-sensing microindentation carried out on similar specimens (see the Supplementary Information). The COVs for microscale

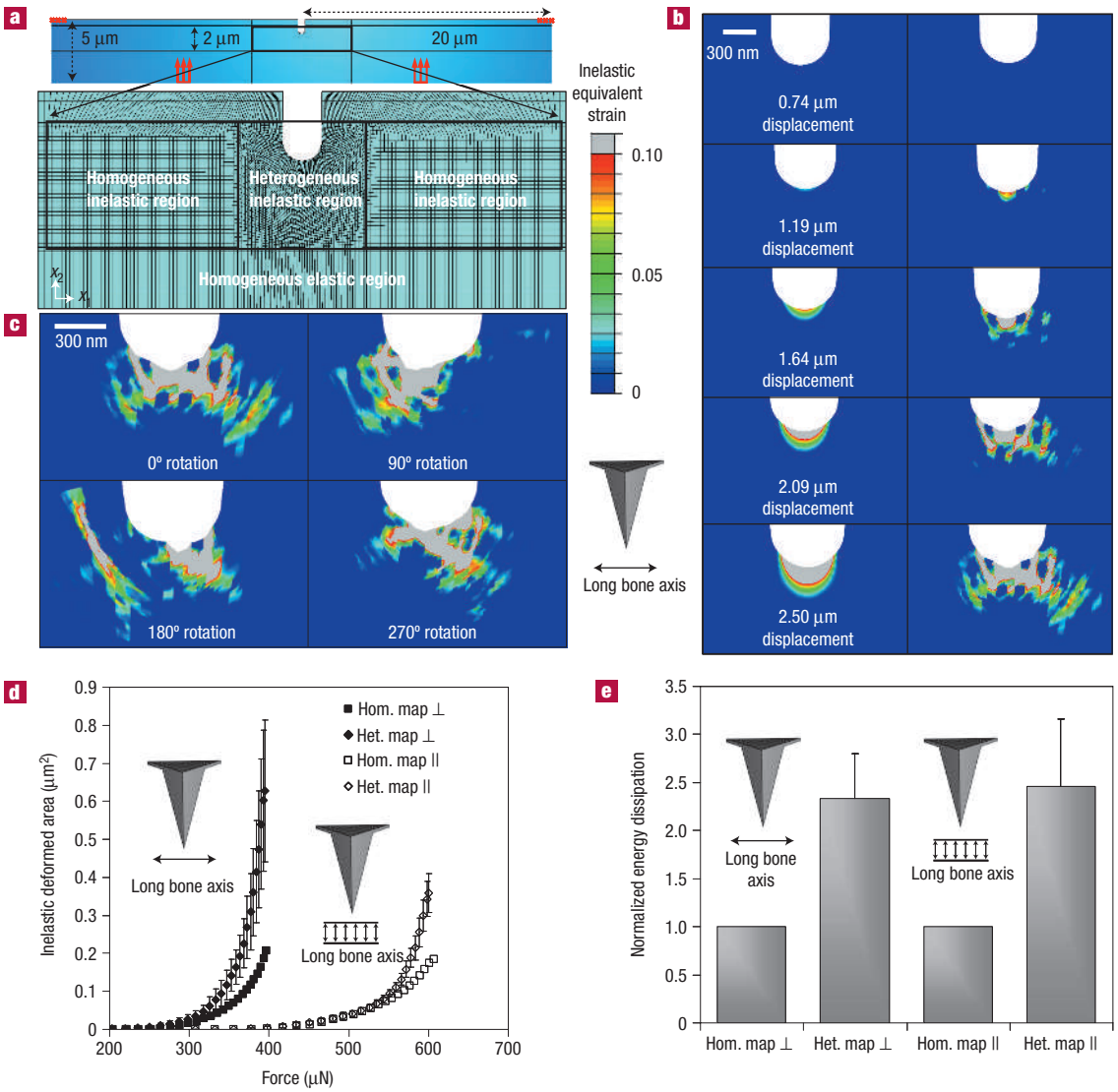

Figure 4 FEA simulations of the effect of nanomechanical spatial heterogeneity on larger-scale biomechanical properties. a, 2D notched four-point bend FEA model geometry showing dimensions and mesh. Modulus maps for adult bovine cortical bone were superimposed in a 2 μm × 2 μm heterogeneous region ahead of the notch. The simulation was displacement controlled with the bottom two boundary conditions (spaced 20 μm apart) displaced 2.5 μm upwards from the bottom whereas the two fixed regions are at the end. Four-node bilinear plane-strain quadrilateral elements (CPE4) were used in this study and the mesh was highly refined in the heterogeneous mapped region. There were 9,424 elements in the 600 nm notched specimen; 3,116 of these elements were within the heterogeneous region. The number of yielded elements was tracked through the equivalent inelastic strain and the reaction force in the vertical direction was measured at the fixed points. Energy dissipation was calculated by integrating the area between the loading and unloading force–displacement curves up to 2.5 μm displacement. **b**, Snapshots of equivalent inelastic strain for the four-point bend FEA virtual simulations comparing the homogeneous to the heterogeneous case for loading up to 2.5 μm. This particular dataset used heterogeneous data with the loading axis perpendicular to the long bone axis (Fig. 2b). **c**, Equivalent inelastic strain for the four-point bend FEA virtual simulations, which incorporated the heterogeneous nanoindentation data taken with the loading axis perpendicular to the long bone axis (Fig. 2b), where the 2 μm × 2 μm map is rotated in the plane of the long bone axis (the plane of the paper) by 0°, 90°, 180° and 270°. **d**, The inelastically deformed area is plotted as a function of force for each set of tests, both perpendicular and parallel to the long bone axis, comparing the homogeneous and heterogeneous cases. The heterogeneous plots are averages of the rotated and shifted contour-mapped regions, indicated by standard error bars ('shifted' simulations involved moving the notch 300 nm vertically upwards and downwards; see Supplementary Information). **e**, Energy-dissipation bar plots for each set of simulations, both perpendicular and parallel to the long bone axis, comparing the homogeneous and heterogeneous cases where the values are normalized to the homogeneous case. The heterogeneous plots are averages of the rotated and shifted contour-mapped regions, indicated by standard error bars. A unit thickness of 1 μm in the 2D model is used to compute the energy dissipation.

indentations (Berkovich geometry at 500 μN maximum load) perpendicular and parallel to the long bone axis were found to be 0.25 and 0.26, respectively (methods are provided in our previous publication[24]). This is markedly less than the nanoscale data presented here, suggesting a scale-dependent homogenization effect. Other studies have reported even smaller microscale COV values of 0.07–0.15 (refs 7,8,32).

To better understand how nanoscale mechanical heterogeneity influences larger-length-scale biomechanical properties, finite-element simulations were carried out using the experimentally

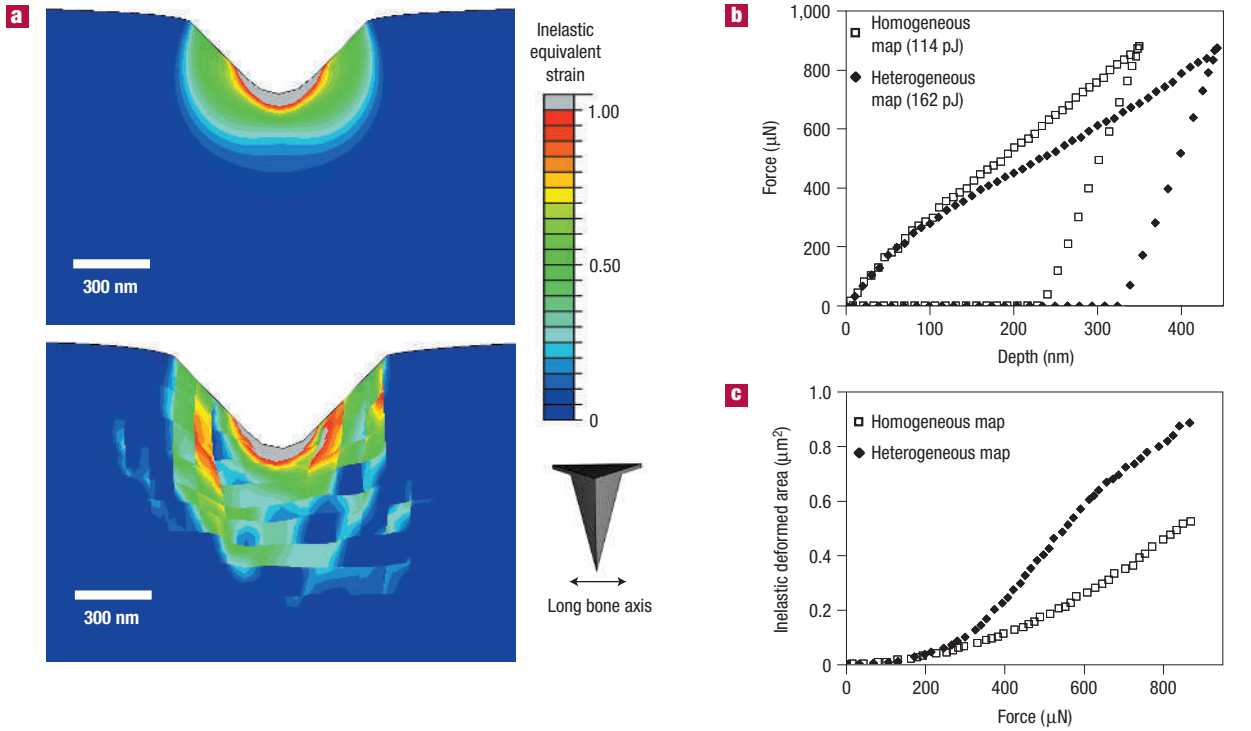

Figure 5 FEA simulations of the effect of nanomechanical spatial heterogeneity on larger-scale compressive loading. a, 2D indentation FEA model showing snapshots of equivalent inelastic strain for an indentation virtual simulation comparing the homogeneous (top) with the heterogeneous (bottom) case for loading up to ~850 μN. This particular dataset used heterogeneous data with the loading axis perpendicular to the long bone axis (Fig. 2b). A unit thickness of 1 μm in the 2D model is used to compute the energy dissipation. **b**, The force–depth curves for the homogeneous and heterogeneous cases. **c**, The inelastically deformed area as a function of force, comparing the homogeneous and heterogeneous cases.

determined fine-scale heterogeneity and local mechanical-property variations extracted from AFM-based indentation experiments. One previous study reported finite-element analysis of a perfectly elastic heterogeneous microstructure on the basis of mean tissue-level experimental data. In that work, the indentation elastic modulus decreased nonlinearly with increasing COV (artificially induced in the simulation). In addition, a marked increase in the number of failed elements (determined by an elastic-limit-strain criterion) was observed with increasing heterogeneity[16]. Here, we directly incorporate the experimentally measured heterogeneous nanoscale-stiffness maps into a highly refined region of finite elements just ahead of a notched four-point bend mesh (Fig. 4a), so as to capture the localization of strain in a region with nanoscale structural non-uniformity. Inelasticity was also incorporated into the four-point bend mesh as follows. Inelastic deformation was first assessed during individual indentation experiments by constructing an axisymmetric 2D FEA simulation with an equivalent tip apex angle of 23.5°, that is, the same indentation volume versus depth as for the AFM probe tip, that assumed a perfect von Mises inelastic constitutive law, as well as a modulus evaluated from the unloading slope[25]. For a number of force-versus-depth indentation curves, various trial yield-stress (σ_Y) values were chosen to determine the optimal value at which the simulated data fitted the experimental curve. Each individual best-fit value (with an average σ_Y value of ~395 MPa) was then used to calculate the corresponding equivalent (elastic) limit strain at the yield point as given by $\bar{\varepsilon}_Y = (2(1+\nu)\sigma_Y)/3E$, where ν is Poisson's ratio and E is the elastic modulus (ν was taken to be 0.25). The $\bar{\varepsilon}_Y$ values were found to be $\sim 0.04 \pm 0.02$ for specimens tested parallel to the long bone axis and $\sim 0.044 \pm 0.02$ for specimens tested perpendicular to the long bone axis. These observations suggest that a constant-elastic-limit-strain (inelastic-yield-strain) criterion is a reasonable first-order approximation. Therefore, taking the above average value of $\bar{\varepsilon}_Y$, the local yield-stress value at each position within the heterogeneous map, σ_Y, can be obtained conversely using $\sigma_Y = (3E\bar{\varepsilon}_Y)/2(1+\nu)$. The energy-dissipative inelastic deformation is incorporated here because a finite residual depth is observed after unloading of the indentation curves (Fig. 2c,f).

Strain-controlled micro- and macro-scale failure of bone has also been studied experimentally using four-point bend specimens with rounded notches[33]. Damage preceding failure was observed to occur immediately at the notch tip (where maximum strain occurs) as opposed to further ahead of the notch tip (where maximum stress occurs), supporting the constant-failure-strain hypothesis. The tensile yield behaviour of bone has also been characterized by critical strain[34]. As noted in earlier work[33], the inelastic constitutive response of bone is at present not fully understood. In compression, nanogranular friction and intraorganic cohesion are thought to be major contributing factors to the inelastic resistance of bone initially[20]. Other mechanisms probably come into play at higher strains owing to the effects of collagen fibril shear[19] and denaturation[24], crack initiation/propagation[33] and sacrificial bond rupture[17]. Although bone is known to show significant tension–compression asymmetry, plasticity models involving the von Mises yield criterion are typically used to capture, at least approximately, the stress/strain fields in bone undergoing inelastic deformation. In the spirit of developing detailed quantitative trends

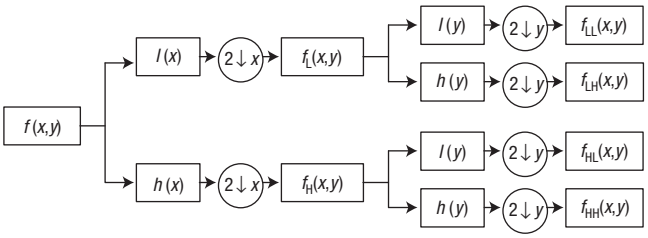

Figure 6 Wavelet decomposition of a 2D image[47]. $f(x, y)$ is the 2D image, $h(x)$ the high-pass filter in the x direction, $l(x)$ the low-pass filter in the x direction, $f_L(x, y)$ the 2D image following the low-pass filter, $f_H(x, y)$ the 2D image following the high-pass filter, $f_{LL}(x, y)$ the 2D image following the low-pass/low-pass filter combination, resulting in the smoothed approximation, $f_{LH}(x, y)$ the 2D image following the low-pass/high-pass filter combination, resulting in the horizontal detail, $f_{HL}(x, y)$ the 2D image following the high-pass/low-pass filter combination, resulting in the vertical detail, $f_{HH}(x, y)$ the 2D image following the high-pass/high-pass filter combination, resulting in the diagonal detail, and $2(\downarrow)x$ the downsampling in the x direction.

for relative assessments of the role of structural heterogeneity from the nano- to the microscale, we invoke, as in earlier studies[33], plasticity analysis (described below) in our finite-element model, with the full realization that comprehensive constitutive models for inelastic deformation of bone have not yet been developed. These simulations, however, are seen to capture key trends of the inelastic deformation of bone when compared with our parallel computational studies that invoke anisotropy and pressure sensitivity of deformation (as noted below).

Figure 4b shows the progression of equivalent inelastic strain (defined as the time integral of $\sqrt{2/3}$ multiplied by the magnitude of the inelastic strain rate) during two virtual four-point bend FEA simulations (displacement controlled). The first (right column) incorporated the heterogeneously mapped data from Fig. 2b (loading axis perpendicular to the long bone axis). The second (left column) was a control, which was an elastic–perfectly plastic simulation with purely homogeneous mechanical properties (set to the volume-averaged mean value of modulus measured experimentally in Fig. 2b and the volume-averaged mean value of yield stress obtained from the strain-based yield criterion). The measured inelastic strain in the vicinity of the notch is continuously greater for the heterogeneous case than the homogeneous from 1.5 to 2.5 μm displacement. The inelastic strain develops irregularly ahead of the notch and extends about twice as far for the heterogeneous material compared with the homogeneous one at 2.5 μm displacement. Non-uniform notch opening and blunting took place in the heterogeneous case, as compared with a more uniform shape change for the homogeneous case. Figure 4c shows the inelastic equivalent strain for the four-point bend FEA simulations at 2.5 μm displacement for the same nanoindentation data (Fig. 2b), where the heterogeneous map ahead of the notch is rotated by 0°, 90°, 180° and 270° in the plane defined by the long bone axis (in the plane of the paper). Although the fine details of the inelasticity pathways are different for different rotations, all simulations show characteristic heterogeneous diffuse deformation over a much greater area compared with the homogeneous material. There is less than 10% variation in the inelastically deformed area for a complete rotation over 360°. The inelastically deformed area as a function of applied force is given (Fig. 4d) for cases both perpendicular and parallel to the long bone axis for both heterogeneous and homogeneous cases. For tests perpendicular to the long bone axis, the inelastically deformed area was about three times as great for the heterogeneous than the homogeneous case at 390 μN maximum force. For tests parallel to the osteonal axis, the inelastic deformation area was about twice as great for the heterogeneous case at 610 μN maximum force. In general, for a 2.5 μm displacement, the inelastic strain region corresponded to an increased applied force for stiffer modulus values, on average. A comparison between maps taken with different loading orientations showed similar energy dissipation, which was about 2.4 times greater for the heterogeneous map compared with the homogeneous case (Fig. 4e). Also, as the notch diameter was varied between 300 and 1200 nm, there was a slight increase (~10%) in the inelastic strain region for heterogeneous and homogeneous cases in both orientations (data not shown). However, the relative ratio of inelastically strained areas between heterogenous and homogeneous cases remained similar.

Further FEA simulations were carried out incorporating anisotropy (using elastic constants from ultrasonic velocity tests[35]) and, separately, pressure sensitivity[20]. These additional simulations (see the Supplementary Information) showed the same overall trends as the foregoing elastoplastic simulations, of increased inelastically deformed area (about threefold) and energy dissipation (about twofold) for the heterogeneous system compared with the homogeneous case. Therefore, although the specific extent of damage evolution and energy dissipation could be somewhat influenced by the particular constitutive model, material anisotropy and pressure sensitivity, it is evident that the overall conclusions extracted from the present computational simulations hold irrespective of the particular choice of material model. Another important issue pertains to the accuracy with which the 2D plane strain model captures the behaviour of the 3D microstructure. Indeed, significant quantitative differences would be expected in the inelastic strain distributions predicted by the 3D model as compared with the 2D case[36,37]. Nevertheless, statistically, inelastic strain and stress (for example maximum principal stress) distributions from a plane-strain model are in general quite similar to those from a full 3D model, with the heterogeneity slightly underestimated by the plane-strain model[36]. These results[36,37] suggest that the plane-strain model used here should be sufficiently accurate to distinguish statistically the relative difference between the heterogeneous case and the homogeneous case.

An additional 2D FEA nanoindentation model was also built with compression as the chief loading mechanism (Fig. 5a). Here, similar to the bending case, the modulus map was superimposed onto a fine mesh with a 90° included-angle indentation geometry to demonstrate that the same trends are observed as with the four-point bend simulations. Figure 5b shows that the simulated force-versus-indentation-depth curves for the homogeneous stiffness map show a smaller deformation for a given load compared with the heterogeneous material (Fig. 2b) for loads larger than ~250 μN. The energy dissipations given by the curves were 114 and 162 pJ for the homogeneous and heterogeneous cases, respectively (for 850 μN maximum load). The inelastically deformed area for the heterogeneous case was markedly greater than that for the homogeneous case (Fig. 5c), consistent with the results obtained from the four-point bending simulations. This result further suggests that, even though heterogeneity at the micro- and macro-scale may have deleterious effects, leading to fracture and interfacial instabilities[38], inelastic heterogeneity at the nanoscale offers an advantageous mechanism for ductile energy dissipation.

In summary, we propose a new energy dissipation mechanism for bone arising from nanomechanical heterogeneity, by recourse to experimental results that provide high-resolution, spatially specific nanomechanical tests in conjunction with detailed computational simulations of locally inelastic deformation. These results provide compelling evidence for enhanced ductility and

energy dissipation through nanoscale structural heterogeneity. This concept is generally applicable to a broad class of natural materials because nanomechanical heterogeneity is expected to be ubiquitously present. In addition, because osteocytes are continually sampling their mechanical environment[39], deformation spread out over greater spatial areas owing to nanomechanical heterogeneity may facilitate damage detection in the extracellular matrix and improved remodelling responses. The heterogeneous nanomechanical patterns measured experimentally would in turn cause corresponding local heterogeneous strains when loaded macroscopically. Such strains are expected to be amplified by the softer surrounding pericellular matrix of osteocytes[40], further affecting cellular processes, possibly acting as 'nanomechanical messages'. Lastly, heterogeneous local strains are also expected to influence interstitial fluid flow, which has been shown to be critical to the proper maintenance of metabolic activity[41].

METHODS

SAMPLE PREPARATION AND CHARACTERIZATION

Samples of adult bovine cortical bone from the proximal tibial metaphysis were prepared as previously described[24]. Sample preparation did not involve chemical treatment, ethanol dehydration or embedding. The mineral content measured by back-scattered electron microscopy was found to be ~58 wt%. The a.c. intermittent contact-mode AFM imaging at ambient temperature and humidity was used with a 3D molecular force probe (MFP-3D, Asylum Research) on hydrated samples of osteonal bone using a silicon etched OMCL-AC160TS (Olympus) rectangular cantilever with a tetrahedral probe tip (cantilever spring constant, $k \sim 56.2\ \mathrm{N\,m^{-1}}$, probe-tip end radius ~15 nm, Fig. 1) in ambient conditions. The tip radius was measured by a.c.-mode imaging of a gold nanoparticle calibration standard[42].

NANOINDENTATION

Nanoindentation experiments were conducted in ambient conditions using the MFP-3D and the same probe tip as that used for a.c.-mode AFM imaging. The inverse optical lever sensitivity and cantilever spring constant calibrations were carried out as previously reported[43]. Displacement-controlled nanoindentation was carried out by loading at a rate of $1\ \mu\mathrm{m\,s^{-1}}$ up to a trigger force of 5 μN followed by unloading at the same rate. The loading/unloading rate was varied from 0.05 to $10\ \mu\mathrm{m\,s^{-1}}$ and no statistically significant differences in calculated moduli were observed at loading rates between 0.5 and $5\ \mu\mathrm{m\,s^{-1}}$, indicating that viscoelastic effects were minimized. The tip contact-area function was calibrated with a sample of glycol methacrylate using a 6 GPa modulus from previous indentation data taken on a Hysitron Triboindentor. Values for elastic moduli were calculated from 95 to 20% of the initial unloading curve by fitting these data to contact mechanical theory for an isotropic, elastic half-space[25] for each individual curve. Due to the assumptions of this model[44,45] (for example isotropy) and the hierarchical nanostructure of bone, the extracted modulus is more appropriately defined as an 'indentation modulus' in that it reflects relative mechanical stiffness and does not produce absolute quantitative values. However, the relative spatial differences in stiffness can be accurately compared. The 100 nm interindent spacing was chosen to be sufficiently large for minimal interference with a neighbouring residual inelastically deformed zone as well as residual stresses, as verified by 2D elastic–inelastic FEA simulations (described in detail in the FEA methods section). Additionally, experimental histogram distributions of the modulus taken at a much larger interindent spacing of 1 μm showed statistically similar modulus distributions ($p < 0.05$). An epoxy control sample (McMaster-Carr) was tested to ensure that the range of stiffness values observed was outside the instrumental scatter and the averaged modulus measured was determined to be 2.9 ± 0.7 with a COV of 0.23.

WAVELET DECOMPOSITION ANALYSIS

Wavelet transform enables localization of both space and frequency, achieved by dilating and translating a finite wavelet function to capture different frequency ranges and their spatial locations[46]. The discrete wavelet transform represents one-dimensional sampled data with a limited number of decomposition levels (frequency scales). A set of low- and high-pass filters is used for decomposing the data into a coarse approximation and a residual detail. Wavelets also enable particular frequency sub-bands to be isolated within an image, which are treated as 2D signals[47]. Figure 6 depicts a one-level decomposition of a 2D image. Filters are applied in the x-direction and the results are down-sampled by deleting every other column. This yields two images of approximately half the size of the original, one containing high-frequency components of the rows and the other containing low-frequency components. These two images are then each filtered down the columns using the corresponding filters and down-sampling the results along the rows. This results in the smoothed-approximation, the horizontal-detail, the vertical-detail and the diagonal-detail subimages. The process is repeated on the smoothed-approximation subimage to obtain the next level of decomposition.

FINITE-ELEMENT ANALYSIS

The elastic contact radius at maximum load (using a threshold of 0.01 logarithmic strain) and the size of the residual inelastic strain zone (using a threshold of 0.01 inelastic equivalent strain) and residual stress zone (using a threshold of 0.1 σ_Y) after unloading were approximated by an elastic–perfectly inelastic 2D axisymmetric-indentation FEA model using the software package ABAQUS (Pawtucket, RI, USA) fitted to individual force–depth curves. The probe-tip geometry was incorporated from direct scanning electron microscopy visualization. The modulus value was fixed to the values obtained from the Oliver–Pharr analysis on the basis of the initial unloading slope[25]. The yield stress was kept as a free fitting parameter, from which the yield strain could be iteratively determined. More detailed discussions on the computational indentation modelling and mechanical property extraction can be found elsewhere[48,49].

A 2D plane-strain four-point bend model (40 μm wide and 5 μm high) was built (Fig. 4a). The experimentally measured modulus maps were incorporated within this FEA model for both specimens with indents perpendicular and parallel to the long bone axis by assigning a specific material section to whichever elements spatially coincided with each particular material region. An elastic-limit-strain-based von Mises plasticity constitutive law was used to model the energy-dissipating inelastic deformation and to obtain a local yield-stress value as described in the main text. The elements in the area immediately to the right and left of the $2\ \mu\mathrm{m} \times 2\ \mu\mathrm{m}$ heterogeneous region were assigned the experimentally measured average homogeneous value of modulus and corresponding yield stress (on the basis of the criterion discussed previously). The elements in the bottom portion were assigned only the purely elastic average homogeneous modulus value.

Received 25 September 2006; accepted 16 April 2007; published 21 May 2007.

References

1. Weiner, S. & Wagner, H. D. The material bone: Structure–mechanical function relations. *Annu. Rev. Mater. Sci.* **28**, 271–298 (1998).
2. Currey, J. Structural heterogeneity in bone: Good or bad? *J. Musculoskelet. Neuronal Interact.* **5**, 317 (2005).
3. Lakes, R. S. Materials with structural hierarchy. *Nature* **361**, 511–515 (1993).
4. Morgan, E. F., Bayraktar, H. H. & Keaveny, T. M. Trabecular bone modulus–density relationships depend on anatomic site. *J. Biomech.* **36**, 897–904 (2003).
5. Pope, M. H. & Outwater, J. O. Mechanical properties of bone as a function of position and orientation. *J. Biomech.* **7**, 61–66 (1974).
6. Skedros, J. G., Sorenson, S. M., Takano, Y. & Turner, C. H. Dissociation of mineral and collagen orientations may differentially adapt compact bone for regional loading environments: Results from acoustic velocity measurements in deer calcanei. *Bone* **39**, 143–151 (2006).
7. Rho, J. Y., Roy, M. E., Tsui, T. Y. & Pharr, G. M. Elastic properties of microstructural components of human bone tissue as measured by nanoindentation. *J. Biomed. Mater. Res.* **45**, 48–54 (1999).
8. Gupta, H. S. *et al.* Mechanical modulation at the lamellar level in osteonal bone. *J. Mater. Res.* **21**, 1913–1921 (2006).
9. Martin, R. B. & Burr, D. B. *Structure, Function and Adaptation of Compact Bone* (Raven, New York, 1989).
10. Rho, J. Y., Zioupos, P., Currey, J. D. & Pharr, G. M. Microstructural elasticity and regional heterogeneity in human femoral bone of various ages examined by nano-indentation. *J. Biomech.* **35**, 189–198 (2002).
11. Balooch, G. *et al.* TGF-beta regulates the mechanical properties and composition of bone matrix. *Proc. Natl Acad. Sci.* **102**, 18813–18818 (2005).
12. Zysset, P. K., Guo, X. E., Hoffler, C. E., Moore, K. E. & Goldstein, S. A. Elastic modulus and hardness of cortical and trabecular bone lamellae measured by nanoindentation in the human femur. *J. Biomech.* **32**, 1005–1012 (1999).
13. Catanese, J. 3rd, Iverson, E. P., Ng, R. K. & Keaveny, T. M. Heterogeneity of the mechanical properties of demineralized bone. *J. Biomech.* **32**, 1365–1369 (1999).
14. Peterlik, H., Roschger, P., Klaushofer, K. & Fratzl, P. From brittle to ductile fracture of bone. *Nature Mater.* **5**, 52–55 (2006).
15. Phelps, J. B., Hubbard, G. B., Wang, X. & Agrawal, C. M. Microstructural heterogeneity and the fracture toughness of bone. *J. Biomed. Mater. Res.* **51**, 735–741 (2000).
16. Jaasma, M. J., Bayraktar, H. H., Niebur, G. L. & Keaveny, T. M. Biomechanical effects of intraspecimen variations in tissue modulus for trabecular bone. *J. Biomech.* **35**, 237–246 (2002).
17. Fantner, G. E. *et al.* Sacrificial bonds and hidden length dissipate energy as mineralized fibrils separate during bone fracture. *Nature Mater.* **4**, 612–616 (2005).

18. Gao, H., Ji, B., Jager, I. L., Arzt, E. & Fratzl, P. Materials become insensitive to flaws at nanoscale: Lessons from nature. *Proc. Natl Acad. Sci. USA* **100**, 5597–5600 (2003).
19. Gupta, H. S. *et al.* Nanoscale deformation mechanisms in bone. *Nano Lett.* **5**, 2108–2111 (2005).
20. Tai, K., Ulm, F.-J. & Ortiz, C. Nanogranular origins of the strength of bone. *Nano Lett.* **6**, 2520–2525 (2006).
21. Currey, J. D. Effects of differences in mineralization on the mechanical properties of bone. *Phil. Trans. R. Soc. Long B* **304**, 509–518 (1984).
22. Currey, J. D. The effect of porosity and mineral content on the Young's modulus elasticity of compact bone. *J. Biomech.* **21**, 131–139 (1988).
23. You, L. D., Weinbaum, S., Cowin, S. C. & Schaffler, M. B. Ultrastructure of the osteocyte process and its pericellular matrix. *Anat. Rec. A Discov. Mol. Cell Evol. Biol.* **278**, 505–513 (2004).
24. Tai, K., Qi, H. J. & Ortiz, C. Effect of mineral content on the nanoindentation properties and nanoscale deformation mechanisms of bovine tibial cortical bone. *J. Mater. Sci.- Mater. Med.* **16**, 947–959 (2005).
25. Oliver, W. C. & Pharr, G. M. An improved technique for determining hardness and elastic modulus using load and displacement sensing indentation experiments. *J. Mater. Res.* **7**, 1564–1583 (1992).
26. Giraudguille, M. M. Twisted plywood architecture of collagen fibrils in human compact-bone osteons. *Calcif. Tissue Int.* **42**, 167–180 (1988).
27. Hofmann, T., Heyroth, F., Meinhard, H., Franzel, W. & Raum, K. Assessment of composition and anisotropic elastic properties of secondary osteon lamellae. *J. Biomech.* **39**, 2282–2294 (2006).
28. Kazanci, M., Roschger, P., Paschalis, E. P., Klaushofer, K. & Fratzl, P. Bone osteonal tissues by Raman spectral mapping: Orientation-composition. *J. Struct. Biol.* **156**, 489–496 (2006).
29. Wagermaier, W. *et al.* Spiral twisting of fiber orientation inside bone lamellae. *Biointerphases* **1**, 1–5 (2006).
30. Ardizzoni, A. Osteocyte lacunar size–lamellar thickness relationships in human secondary osteons. *Bone* **28**, 215–219 (2001).
31. Mallat, S. *A Wavelet Tour of Signal Processing* (Academic, San Diego, 1998).
32. Donnelly, E., Baker, S. P., Boskey, A. L. & van der Meulen, M. C. H. Effects of surface roughness and maximum load on the mechanical properties of cancellous bone measured by nanoindentation. *J. Biomed. Mater. Res. A* **77**, 426–435 (2006).
33. Nalla, R. K., Kinney, J. H. & Ritchie, R. O. Mechanistic fracture criteria for the failure of human cortical bone. *Nature Mater.* **2**, 164–168 (2003).
34. Currey, J. D. Tensile yield in compact bone is determined by strain, post-yield behaviour by mineral content. *J. Biomech.* **37**, 549–556 (2004).
35. Rho, J. Y. Ultrasonic method for measuring elastic properties of human tibial cortical and cancellous bone. *Ultrasonics* **34**, 777–783 (1996).
36. Böhm, H. J. & Han, W. Comparisons between three-dimensional and two-dimensional multi-particle unit cell models for particle reinforced metal matrix composites. *Modell. Simul. Mater. Sci. Eng.* **9**, 47–65 (2001).
37. Shen, H. & Lissenden, C. J. 3D finite element analysis of particle-reinforced aluminum. *Mater. Sci. Eng. A* **338**, 271–281 (2002).
38. Nakamura, T. & Suresh, S. Effects of thermal residual-stresses and fiber packing on deformation of metal-matrix composites. *Acta. Metal. Mater.* **41**, 1665–1681 (1993).
39. Ehrlich, P. J. & Lanyon, L. E. Mechanical strain and bone cell function: A review. *Osteoporos. Int.* **13**, 688–700 (2002).
40. You, L., Cowin, S. C., Schaffler, M. B. & Weinbaum, S. A model for strain amplification in the actin cytoskeleton of osteocytes due to fluid drag on pericellular matrix. *J. Biomech.* **34**, 1375–1386 (2001).
41. Burger, E. H. & Klein-Nulend, J. Mechanotransduction in bone—role of the lacuno-canalicular network. *FASEB J.* **13** (suppl), S101–S112 (1999).
42. Vesenka, J., Manne, S., Giberson, R., Marsh, T. & Henderson, E. Colloidal gold particles as an incompressible atomic force microscope imaging standard for assessing the compressibility of biomolecules. *Biophys. J.* **65**, 992–997 (1993).
43. Seog, J. *et al.* Direct measurement of glycosamnoglycan intermolecular interactions via high-resolution force spectroscopy. *Macromolecules* **35**, 5601–5615 (2002).
44. Oliver, W. C. & Pharr, G. M. Measurement of hardness and elastic modulus by instrumented indentation: Advances in understanding and refinements to methodology. *J. Mater. Res.* **19**, 3–20 (2004).
45. Pharr, W. C. O. Indentation of an elastic planar substrate by solid. *J. Mater. Res.* **7**, 1564 (1992).
46. Strang, G. & Nguyen, T. *Wavelets and Filter Banks* (Wellesley-Cambridge, Wellesley, MA, 1996).
47. Tsai, D. M. & Hsiao, B. Automatic surface inspection using wavelet reconstruction. *Pattern Recognition* **34**, 1285–1305 (2001).
48. Dao, M., Chollacoop, N., Van Vliet, K. J., Venkatesh, T. A. & Suresh, S. Computational modeling of the forward and reverse problems in instrumented sharp indentation. *Acta Mater.* **49**, 3899–3918 (2001).
49. Gouldstone, A. *et al.* Indentation across size scales and disciplines: Recent developments in experimentation and modeling. *Acta Mater.* **55**, (2007, doi:10.1016/j.actamat.2006.08.044).
50. Thurner, P. *et al.* High-speed photography of compressed human trabecular bone correlates whitening to microscopic damage. *Eng. Fracture Mech.* **74**, 1928–1941 (2007).
51. Landis, W. J. The strength of a calcified tissue depends in part on the molecular structure and organization of its constituent mineral crystals in their organic matrix. *Bone* **16**, 533–544 (1995).
52. Wachtel, E. & Weiner, S. Small-angle X-ray scattering study of dispersed crystals from bone and tendon. *J. Bone Miner. Res.* **9**, 1651–1655 (1994).

Acknowledgements

The authors thank the MIT Department of Materials Science and Engineering Nanomechanical Testing Facility, The Whitaker Foundation and the US Army through the MIT Institute for Soldier Nanotechnologies (contract number DAAD-19-02-D0002), and the NIH grant 1-R01-GM076689-01 on multiscale modelling for funding. M.D. and S.S. also acknowledge partial support from the United States Army Research Office and the Joint Improvised Explosive Devices Defeat Organization under contract number W911NF-07-1-0035. The content does not necessarily reflect the position of the government and no official endorsement should be inferred. The authors would also like to thank graphic artist Beryl Simon for preparation of Fig. 2g.
Correspondence and requests for materials should be addressed to C.O.
Supplementary Information accompanies this paper on www.nature.com/naturematerials.

Competing financial interests

The authors declare no competing financial interests.